Lee Yuni (Orcid ID: 0000-0003-0463-7650)
Fang Xiaohua (Orcid ID: 0000-0002-6584-2837)
Gacesa Marko (Orcid ID: 0000-0001-5145-051X)
Ma Ying Juan (Orcid ID: 0000-0003-2584-7091)
Mahaffy Paul, R. (Orcid ID: 0000-0003-1896-1726)
Dong Chuanfei (Orcid ID: 0000-0002-8990-094X)
Combi Michael R. (Orcid ID: 0000-0002-9805-0078)
Bougher Stephen, W. (Orcid ID: 0000-0002-4178-2729)
Jakosky Bruce, M. (Orcid ID: 0000-0002-0758-9976)

Effects of Global and Regional Dust Storms on the Martian Hot O Corona and Photochemical Loss

Yuni Lee[1,2], Xiaohua Fang[3], Marko Gacesa[4,5], Yingjuan Ma[6], Valeriy Tenishev[7], Paul Mahaffy[1],

Chuanfei Dong[8], Michael Combi[7], Stephen Bougher[7], and Bruce Jakosky[3]

[1]NASA Goddard Space Flight Center, USA
[2]University of Maryland Baltimore County, CRESST II, USA
[3]Laboratory for Atmospheric and Space Physics, University of Colorado Boulder, USA
[4]Space Science Division, NASA Ames Research Center, Moffett Field, California, USA
[5]Bay Area Environmental Research Institute (BAERI), Moffett Field, California, USA
[6]Department of Earth, Planetary, and Space Sciences, University of California, Los Angeles, USA
[7]Climate and Space Sciences and Engineering Department, University of Michigan, Ann Arbor, MI, USA
[8]Department of Astrophysical Sciences and Princeton Plasma Physics Laboratory, Princeton University, Princeton, NJ, USA

*Corresponding author: yuni.lee@nasa.gov

Key points:

- We investigated the effect of dust storms on photochemical escape from Mars using up-to-date cross sections for O-CO_2 collisions.
- The storm-induced upward shift of the ionosphere causes increased production of hot O and efficient thermalization occurs by the inflated thermosphere.
- The net result is a global photochemical escape rate that is suppressed by ~28% during the global dust storm scenario.

Manuscript prepared for submission to Journal of Geophysical Research: Space Physics – Special issue

Abstract

We examine here for the first time the effects of both global and regional dust storms on the formation of the Martian hot O corona and associated photochemical loss of O. Our study is conducted by utilizing our integrated model framework, which couples our Martian hot O corona model with a multifluid magnetohydrodynamic model for Mars for the dusty and clear atmospheric condition cases. We present our results with the most up-to-date cross sections for the $O(^3P)$-CO_2 collisions. The main effect of dust storms on the ionosphere is the upward shift of the ionosphere on the dayside, which results in an increase in production of hot O at all altitudes above the ionospheric peak. However, the dust-induced inflation of the neutral upper atmosphere results in an enhancement in collisional loss of hot O and thus effectively suppresses the hot O density, reducing the global photochemical loss rate by ~28% for the global dust storm scenario. The relative density structure of the hot O corona does not show any significant changes, while its magnitude decreases at all altitudes.

1. Introduction

The coupling between the Mars lower and upper atmosphere allows lower atmospheric processes to drive forcing in the upper atmosphere. In particular, the enhanced dust loading in the lower atmosphere during dust storms has profound effects on the dynamics, energy balance, and structure of the upper thermosphere and ionosphere [*Bougher et al.*, 1997]. Dust is in fact widely spread in the Mars' atmosphere. Even in absence of storms during the quiet period of the year, dust optical depth remains relatively large (~0.5). While the lower atmosphere is dominated by the dust lifted from the Martian surface, dust found in the upper atmosphere originates predominantly from interplanetary sources and partly from the planet's natural satellites (*i.e.*, Phobos and Deimos) [*Andersson et al.,* 2015; *Pabari and Bhalodi*, 2017]. Earlier observations of

the spatial and seasonal changes of the dust [*e.g.*, *Briggs et al.*, 1979; *Thorpe*, 1979, and references therein] have shown that typical regional dust storms always occur when Mars is near its perihelion, while the occurrence of global dust storms (*e.g.,* dust storm observed by Viking in 1971 and 1972) is quite rare – Unlike global dust storms, the planet-encircling dust events (PEDEs) are observed to occur every 3-4 Martian years.

Dust storms at Mars are known as the most phenomenal meteorological process as well as the most radiatively important element. However, the physical mechanisms and dynamics as well as their effects on the Martian climate still remain questionable. When a planet-encircling dust storm occurs, the storm can engulf the entire planet within some range of the equator with a haze of dust and have planet-wide impacts on the atmosphere for several months. Dust suspended during global storms can lead to cooling of the surface, radiative heating by lifted dust aerosol from the surface, lofting of the lower atmosphere and modification of the atmospheric circulation, which in turn influence the chemistry and climate of Mars [*Vandaele et al.,* 2019]. In contrast, regional storms last for only a few sols over small defined areas, and the frequency of these storms decreases with increasing surface area covered by the storms [*Cantor et al.*, 2001]. Impacts of regional storms are relatively mild compared to global storms. Previous modeling studies have suggested that a positive feedback process can occur between local dynamics and radiative forcing of regional dust disturbances under some conditions, which is different from the feedback by enhanced atmospheric dust loading [*Rafkin*, 2009].

The effects of dust storms on the ionosphere and thermosphere also imply their direct impacts on the exosphere. The variability of ionosphere and thermosphere is critical to the formation of the Martian hot atomic coronae [*e.g.*, *Cravens et al.*, 2017; *Fox and Hać*, 2009, 2014; *Gröller et al.*, 2014; *Lee et al.*, 2015b; *Lillis et al.*, 2017; *Rahmati et al.*, 2017; *Valeille et al.*, 2009a, 2009b; *Yagi et al.*, 2012]. In particular, the hot O corona at Mars is produced mainly by the dissociative recombination reaction of O_2^+ with electrons, which is a photochemical reaction [*e.g.*, *Fox and Hać*, 2009; *Nagy et al.*, 2001], with most of the hot O production taking place deep in the ionosphere and thermosphere. Thus, any temporal and spatial variability in the ionosphere and thermosphere will lead to perturbations in the escaping process of hot O. The degree of impacts highly depends on factors such as altitude and competition between the processes which produce fast O atoms and those (mostly collisions) which reduce their energies.

Here, we investigate, for the first time, global and regional dust storm effects on the formation of the Martian hot O corona and the escaping process of hot O to space. This study utilizes a one-way coupling method to model the impact on hot O structure and escape rates on ionospheric and thermospheric variability during dust storms. This study is designed to advance our understanding of the variability of the Martian exospheric population and photochemical loss rate, with the dust storm impact considered. In section 2, we describe our numerical models, the coupling procedure, and the O-CO_2 collision cross sections. Section 3 provides an overview of the thermospheric and ionospheric conditions adopted in our hot O corona simulations. In section 4, we present our results from the cases considered in this study and conclude in section 5.

2. Model Descriptions

2.1 Adaptive Mesh Particle Simulator (AMPS)

The numerical tools that we use to investigate the dust storm effects on the formation of the hot O corona and photochemical loss process are our 3D kinetic particle simulator and 3D multifluid MHD model. The main numerical tool for this study, our state-of-the-art 3D Adaptive Mesh Particle Simulator (AMPS) [*Tenishev et al.*, 2008, 2011, 2013], is a kinetic particle model, which is developed within the frame of the Direct Simulation Monte Carlo (DSMC) method [*Bird*, 1994] and employs a stochastic solver for both the linear and nonlinear Boltzmann equations. AMPS is generic and well-tested code for various kinetic problems in rarefied gas flow regime, including the gas and dust distributions in cometary comas [*Rubin et al.*, 2011; *Fougere et al.*, 2012; *Tenishev et al.*, 2008, 2011; *Combi et al.*, 2012; *Bieler et al.*, 2015; *Bockelée-Morvan et al.*, 2015; *Fougere et al.*, 2016a, b], the plumes of Enceladus [*Waite et al.*, 2006; *Tenishev et al.*, 2010, 2014], and the exosphere of the Moon [*Tenishev et al*., 2013].

Within the model, ensembles of model particles are simulated to capture the macroscopic parameters of the gas distribution. The model describes the collisional dynamics of a finite number of model particles in a rarefied gas flow regime, allowing a realistic description for the transition region between collision-dominated and collisionless regimes. Our application of AMPS to the Martian exosphere simulates the formation of hot neutral coronae and computes the consequent loss of the neutral species. Each model particle moves under the influence of the

gravitation field of Mars and collides with ambient thermospheric particles before it completely escapes to space or become thermalized in the model domain. The full technical specification of the AMPS code as well as a detailed description of its application to the Martian exosphere are given by *Tenishev et al.* [2008, 2013] and *Lee et al.* [2014a, 2014b, 2015a, 2015b], respectively.

2.2 Multi-fluid Magnetohydrodynamic model (MF-MHD)

Our hot O corona simulations are based on the input thermospheric and ionospheric descriptions. We incorporated into the AMPS code the dust storm effects in our input ionosphere, where ion dynamics and chemical processes are solved using the 3D BATS-R-US Mars multifluid MHD (MF-MHD) model [*Najib et al.*, 2011; *Dong et al.*, 2014, 2015]. The MF-MHD model for Mars simulates the structure and dynamics of the ionosphere self-consistently, with the lower boundary of the model extending down to such an altitude that the majority of the ionosphere is covered (~100 km). The crustal magnetic field is prescribed by using an expansion of spherical harmonic functions developed by *Morschhauser et al.* [2014] up to the degree of 110. To describe both the dust-disturbed and non-disturbed conditions of the ionosphere by the dust storms, we focused on the dust storm effects that result from the inflation of thermosphere due to the increase in dust loading of the lower atmosphere of Mars. The thermospheric conditions for the dusty and clear atmospheric condition cases for each storm are described in Section 3 as well as *Fang et al.* [2019]. Detailed descriptions of model parameters in the MHD simulations of dust storm effects on the Martian plasma environment are provided by *Fang et al.* [2019]. This study

provides brief descriptions of model parameters and underlying assumptions that are relevant only to the formation of the hot O corona and photochemical escape process.

2.3 Integrated Model Framework

The AMPS and MF-MHD models are coupled in one direction only, such that our AMPS code incorporates pre-simulated results from the MF-MHD model for the cases considered without transferring the feedback for updating the MF-MHD's computation. This one-way model integration between the AMPS and MF-MHD models has been carried out by our previous studies but with different input thermospheric and ionospheric conditions for the different aims of the studies [*e.g.*, *Dong et al.*, 2015, 2018; *Lee et al.*, 2018a]. Among the processes that can be described by the feedback between the AMPS and MF-MHD models is, for example, sputtering process via pickup ions. The MF-MHD model can generate the electric and magnetic fields and particle precipitation rates needed for computation of sputtering of neutral atoms by pickup ions. Using these information, the AMPS model can update its calculation of exospheric O, which then can be provided to the MF-MHD model. Another example, which is more relevant to the scope of this study, is a simultaneous calculation of the hot O corona and ionosphere by the AMPS and MF-MHD models, respectively. As this has not been achieved yet in the current one-way integration procedure, the MF-MHD model assumes a 1D hot O corona in its initial calculation (*i.e.,* globally averaged hot O corona from the literature is distributed spherically symmetrically over the globe in the computational domain). This assumption has been used in

the previous MHD modeling studies [*e.g., Ma et al.,* 2004; *Dong et al.,* 2014], which produced observations reasonably well.

Figure 1

Our model integration procedure is illustrated in Figure 1. To summarize the procedure, we take following steps to reach our final simulation results:

1) Initial simulation by the MF-MHD model for the cases for disturbed (*i.e.,* dusty) and undisturbed (*i.e.,* clear) atmospheric conditions. The input thermosphere describes the disturbed and undisturbed atmospheric conditions, and the input hot O corona is the assumed spherically symmetric hot O corona from literature.

2) Initial simulation by the AMPS model for the cases considered, using resulting ionosphere from the initial run by the MF-MHD model in step 1. The thermospheric inputs are the same as the ones used in step 1 in the MF-MHD model.

3) Second simulation by the MF-MHD model for the cases considered, using the same thermospheric inputs. The hot O corona simulated in step 2 by the AMPS mode is globally averaged and supplied to the MF-MHD model.

4) Second simulation by the AMPS model for the cases considered, using the same thermospheric inputs and the resulting ionospheres in step 3 by the MF-MHD model.

The resulting hot O corona and estimated photochemical loss rate from Step 4 are our final simulation results.

The integration of our AMPS and the MF-MHD models allows us to achieve our main objectives, which are to 1) incorporate the effects of dust storms on the ionosphere in the formation of the hot O corona and photochemical escape process, and to 2) include self-consistently described ion dynamics and chemical processes due to the inflated thermosphere and ionosphere by dust storms. This study considers the dissociative recombination reaction of O_2^+ only as a source of hot O. AMPS also takes into account hot O created from collisions between thermospheric O and hot O. This collisional source of hot O occurs when the thermospheric O gains enough energy after colliding with hot O and meets the hot O criterion in our model domain – we define a model particle as a hot O particle if its speed exceeds twice of the local thermal speed.

2.4. O-CO$_2$ Collision Cross Sections

For all simulations, we considered O and CO_2 only as the background thermospheric species as information for other major thermal species (e.g., CO and N_2) are not available for our global dust storm scenario. Thus, we assumed that collisions between hot O and other thermospheric species, which were considered in our previous modeling studies for nominal thermospheric and ionospheric conditions [*e.g., Lee et al.,* 2015] for different solar activity levels and distances between Sun and Mars, do not modify significantly the velocity distribution of hot

O. According to our previous studies, the effects of including CO and N_2 in the background gas may be as large as ~30% decrease in the resulting escape rate.

As the Martian atmosphere is composed mainly of O and CO_2, the resulting hot O density and photochemical escape rate are highly sensitive to the assumption of collision types and cross sections. Therefore, a careful treatment of the O-CO_2 collision process is needed to accurately simulate the photochemical escape process of hot O from Mars. Prior to the newly calculated velocity- and angle-dependent $O(^3P)$-CO_2 collision cross sections by *Gacesa et al.* [2019a, 2019b], our previous studies of the Martian hot O corona have adopted the same angular dependency of the scattering as in the O-O collision cross section [*Kharchenko et al.,* 2000] for O-CO_2 collision with an assumed integrated total cross section. The estimated OI 130.4nm brightness derived from the resulting hot O coronal density did not agree well with the observed brightness by the Imaging Ultraviolet Spectrograph (IUVS) [*McClintock et al.,* 2014] instrument onboard MAVEN [*Lee et al.*, 2015a]. Our preliminary study of *Lee et al.* [2018b] has shown that the model-data comparison can be considerably improved by using the total cross section (*i.e.*, elastic and inelastic cross section) by *Gacesa et al.* [2019a, 2019b]. Thus, in this study, we adopted the most recent angle- and energy-dependent differential cross section by *Gacesa et al.* [2019a, 2019b] and assumed that all collisions involve $O(^3P)$. This is a reasonable assumption given the fact that more than 70% of hot O produced in dissociative recombination of O_2^+ with electrons is $O(^3P)$ and the oxygen atoms produced in their excited states (predominantly as $O(^1D)$)

have a high chance to decay to their ground state before interacting with thermal species [*Kharchenko et al.*, 2000].

The new cross sections were calculated from first principles using three newly constructed *ab-initio* potential energy surfaces correlating to the lowest energy asymptote of the $O(^3P)+CO_2$ complex, where CO_2 is represented as a linear rigid rotor. *Gacesa et al.* [2019a, 2019b] obtained excellent agreement with potential energy surfaces reported by *de Lara-Castells et al.* [2006], where applicable. Quantum-mechanical coupled-channel formalism with a large basis set, as implemented in MOLSCAT code [*Hutson and Green*, 1994], was used to compute state-to-state cross sections for $O(^3P)+CO_2$ scattering in a restricted planar geometry. A detailed report of the investigation of the electronic structure of $O(^3P)+CO_2$ complex and construction of scattering cross section is given by *Gacesa et al.* [2019a, 2019b].

Figure 2

Figure 2 shows three different sets of O-CO_2 differential cross sections used in our hot O corona simulations. In this study, unless specified otherwise, we adopted the cross sections by *Gacesa et al.* [2019a, 2019b] at the collision energy of 2.5 eV, corresponding to the dominant production channel of hot O through dissociative recombination (DR) [*Fox and Hać*, 2009]. Although we did not take into account the full energy-dependent cross section in this study, our choice of cross sections at a single collision energy also produces reasonable photochemical loss as the integrated total cross sections do not vary significantly at collision energies that are

relevant to escaping O atoms. Specifically, the integrated total cross sections varies by only about 15% between the escape energy for O (*i.e.,* ~1.98 eV at 200 km) and ~3.5 eV, which is exothermicity of the other important channel in O_2^+ DR that can produce escaping O atoms. This difference will result in approximately less than a 10% change in the resulting escape rate.

The total cross section shown in Figure 2 is defined as a sum of elastic and inelastic cross sections, where the inelastic cross sections considers internal excitations of ground state of the CO_2 molecule. As shown, all three differential cross sections are characterized by a large forward scattering peak at small angles (*i.e.,* < ~5°) and relatively small cross sections at larger angles. The newly adopted differential cross section shows that small scattering angles are dominated by elastic collisions, whereas inelastic collisions are predominant at larger scattering angles. The momentum transfer in collisions does not occur at small angles, whereas scatterings at larger angles facilitate efficient thermalization of hot O. This, in turn, points out that, when using our new $O-CO_2$ collision cross section, most of the thermalization of hot O via collisions with CO_2 favors the transfer of a significant fraction of kinetic energy from hot O to the internal excitation of the CO_2 molecule. In this study, however, we did not take into account the energy loss of hot O to the internal excitation of the CO_2 molecule for two reasons: 1) detailed information (*e.g.,* state-to-state energy transfer data to the CO_2 molecule) is not yet available in a suitable form to be included in our modeling work, 2) our preliminary calculations show that the hot O energy transfer to the internal excitation of the CO_2 molecule would have only small effect on the resulting hot O escape rate and density. If the effect is included, the expected decrease in the

resulting hot O escape rate and density is estimated to be at most ~10% for ~2.5 – 3.5 eV collision energies. Moreover, the differential cross sections are more than about 5 orders of magnitude smaller at large angles, where the process is efficient, than the forward scattering peak at small angles. A detailed description of inelastic collisions in our modeling will be considered in our future studies.

As an academic exercise, we examined the impacts of choice of different O-CO_2 collision cross section on the resulting photochemical escape rate. We used the cross sections shown in Figure 2, which are 1) angular dependency of elastic O-O collisions and an integrated cross section of 2×10^{-18} cm^2 (KH), 2) elastic only O-CO_2 collision cross section by Gacesa et al. [2019a, 2019b] (GE), and 3) total (elastic plus inelastic) O-CO_2 collision cross section by Gacesa et al. [2019a, 2019b] (GT). The only purpose of this exercise is to study the impacts of ignoring inelastic scattering in the O-CO_2 collision.

3. Thermosphere and Ionosphere Conditions

3.1. Thermospheric Conditions

We assume that the primary responses to dust storms come from the thermospheric constituents. The disturbed thermospheric condition affects the ionosphere through ion-neutral coupling and chemical reactions, including photoionization and electron impact ionization, and affects the exosphere mainly through collisions. As dominant species in the upper atmosphere of Mars, the thermospheric O and CO_2 are the major collision partners of the nascent hot O atoms.

The net effects of dust storms on the escaping hot O population will depend on the interplay between the disturbed ionosphere (which is the source of the hot O) and the thermosphere (which can thermalize the hot O). Hence, it is important to adopt reasonable thermosphere inputs to explore the role of dust storms on the photochemical loss process.

Figure 3

Figure 3 shows the background thermosphere adopted in our hot O corona model for the cases considered for this study. The thermospheric input for each case was generated by distributing spherically symmetrically the same thermospheric profiles adopted in the MF-MHD model. The density profiles of O and CO_2 for the global dust storm scenario were established by directly adopting the thermospheric density profiles from *Wang and Nielsen* [2003], which describes the conditions during the 1971-1972 global dust storm. For the regional dust storm scenario, the thermospheric density profiles were constructed by fitting the averaged observations taken by the Neutral Gas and Ion Mass Spectrometer (NGIMS) instrument [*Mahaffy et al.,* 2014] onboard the Mars Atmosphere and Volatile EvolutioN (MAVEN) mission [*Jakosky et al.,* 2015] during the 2017 regional dust storm period. The fitted profiles were extrapolated to the lower and higher altitude regions to provide the thermospheric input to both the MF-MHD and AMPS models. Detailed procedure and specification of the dusty and clear atmospheric condition cases for both storm scenarios are described in *Fang et al.* [2019].

As mentioned earlier, the MF-MHD pre-simulated the disturbed ionospheric condition during dust storms as a response to the inflated thermosphere in the lower atmosphere. Besides the thermosphere, another input parameter to the MF-MHD simulation is the hot O corona. The hot O corona density dominates over the thermal O density at altitudes between ~400 and 600 km, varying with the underlying thermospheric and ionospheric conditions. The cross-over altitude from the thermal-O-dominated atmosphere to the nonthermal-O-dominated atmosphere occurs at ~510 km and ~490 km for the dusty and clear atmospheric condition cases for the global dust storm case, respectively, and ~420 km and ~380 km for the dusty and clear atmospheric condition cases for the regional dust storm case, respectively. In order to take this into account, the input O density profile to the MF-MHD model in the step 2 of our coupling procedure (Figure 1) were modified by using the hot O corona from the AMPS model.

3.2. Modeled Response in the Ionosphere

Figures 4a and 4b show the electron and O_2^+ densities at SZA 30° extracted from the simulated ionosphere by the MF-MHD model, respectively, for both the global and regional dust storms scenarios. These profiles represent approximately the values between the one at the subsolar location and the dayside-averaged one. The main response of the ionosphere to dust storms is the upward altitude shift of the ionosphere. The entire ionosphere is vertically shifted upward by about 15 km for the global dust storm case, while the shift is relatively small for the regional dust storm (~7 km). As the dust storm progresses globally, the increase of the dust

aerosol induces the radiative heating in the lower atmosphere, resulting in the increases of the ionospheric density at all altitudes above the ionospheric peak in our clear atmosphere case. A detailed examination of the dust-induced perturbations in the ionosphere and induced magnetosphere during these regional and global dust storms has been given by *Fang et al.* [2019]. The shift of the ionosphere results in the global enhancement of the hot O production at all altitudes above the pre-storm peak of the ionosphere.

Figure 4

4. Results

4.1 Response of the Hot O Corona

Figure 5 shows the noon-midnight meridional plane view of the simulated hot O corona for the dusty and clear atmospheric condition cases for the global dust storm scenario. Overall, the storm does not alter the spatial structure of the hot O corona (Figure 5a). The shape of the dayside and nightside of the coronal envelope is preserved when the dust storm effects are implemented in the simulation. Similarly, the regional dust storm also does not affect the shape of the hot O corona (Figure 6a). Although the entire ionosphere is lofted, which is the source region of the hot O, the arising hot O corona does not show any prominent inflation of its envelope.

Figure 5

On the other hand, the magnitude of the hot O density changes as we apply the dust storm effects on the ionosphere and thermosphere. Especially, the change in the density is dramatic in the global storm scenario, whereas the change is not significant in the regional dust storm scenario. Both the global and regional storms derive enhancement of the hot O production as the dissociative recombination of O_2^+ rate at altitudes above the ionospheric peak increases. However, the resulting hot O density decreases at all altitudes when storm effect is applied. As displayed in Figure 5a and 6a, the average decrease in density are about ~42 % and ~7 % for the global and regional dust storm scenarios, respectively. The response of the thermosphere to the storms more than compensates for the "puffing up" of the ionosphere, resulting in a net suppression of the hot O corona. Thus, we see that the formation of the hot O corona is highly sensitive to the balance between responses of ionosphere and thermosphere to the dust storms.

Figure 6

Figure 7 shows the globally-averaged hot O density as a function of altitude for the cases considered in this study. For the global dust storm cases, the maximum density of hot O is reached at 240 km and 230 km for the dusty and clear cases, respectively. Due to the upward shift of the ionosphere during dust storms (as shown in Figure 3), the peak altitude of the hot O

production is also shifted to a higher altitude compared to the clear case. In our model case for the global dust storm, the resulting hot O density peak altitude for the dusty case is located ~10 km higher altitude than for the clear case. The density ratio between the dusty and clear cases is the largest at low altitudes (<~200 km) and stays almost constant at high altitudes (<~550 km). Due to intense thermalization of hot O at low altitudes, the hot O density is a factor of about 2 smaller in the dusty case for altitude below ~600 km, compared to the clear case. For the regional dust storm, the peak altitude of the hot O density is located at 240 km and 220 km for the dusty and clear cases, respectively. As in the cases for the global dust storm, the peak altitude of the hot O density for the dusty case is higher than that in the clear case. The difference in the hot O density can be seen only at altitudes near the peak density altitudes as the inflation of the thermosphere in the regional dust storm case is not significant (Figure 4). At these altitudes, the dust storm effects are difficult to detect, since the exospheric O density is dominated by thermal O density.

Figure 7

4.2. Response of Photochemical Escape

Table 1 summarized the global escape rate of hot O for the cases considered in this study. Based on the estimations from our modeling efforts, photochemical escape of O is reduced during dust storms. The decrease depends on the intensity and size of the storm. In our global

dust storm cases, the escape rate decreases by ~28 % for the dusty case, compared to the clear case. The decrease of the escape rate for the regional dust storm cases is not as considerable as the global dust storm cases as the effects of regional dust storms on the ionosphere and thermosphere are not significant. As mentioned earlier, this decrease of photochemical escape of O is achieved by the efficient thermalization of hot O by the inflated thermosphere.

Table 1

The resulting escape rates in Table 1 also show variations of escape rates by the choice of the O-CO_2 collision cross section. As mentioned earlier (Section 2.4), three sets of simulation cases are carried out to examine the sensitivity of the hot O escape to the O-CO_2 collision cross section. The GE case here is unrealistic because we assume only elastic scattering process. Therefore, this academic exercise allows us to explore only the impacts of ignoring inelastic scattering between the hot O atom and the CO_2 molecule.

The escape rate appears to be the highest for the elastic collision cross section only case (GE). In that case, thermalization of hot O does not occur as efficiently as in the KH or GT case, mainly due to relatively small values of differential cross sections at large scattering angles. Because of the highly concentrated forward scattering in the GE case, the inflated thermosphere does not play an important role in the thermalization of hot O. Consequently, the resulting dust storm effect (for both global and regional dust storm scenarios) is the opposite of when KH or

GT is employed, resulting in an increase in the hot O density and escape rate for the dusty cases. The difference in O escape rates between the KH and GT cases is attributed to the artificially imposed integral cross section in the KH case, which is greater than the integral cross section for the GT case, as well as to a large forward scattering peak present in the GT case.

4.3. Escape Probability of Hot O

Figure 8

We have computed the escape probabilities of hot O atoms based on our ionospheric and thermospheric inputs for the cases considered. We did not account for the collisional source of hot O (*i.e.*, the secondary hot O) in our probability calculation in order to consider only the production of hot O from the main photochemical source. The secondary escape due to collisions of hot O with other O-bearing species, such as OH [*Gacesa et al.,* 2017], are expected to contribute at most a few percent and were also not included. Figure 8a shows the computed escape probabilities at a solar zenith angle of 10° for the dusty and clear cases for the global and regional dust storm scenarios as a function of altitude. Generally, the probability of hot O escape increases with altitude as neutral density decreases, and reaches 0.5 rapidly above an altitude at which the probability becomes ~0.1. In the global storm scenario, the increase in production of hot O is larger than that in the regional storm scenario, but the thermalization of hot O is more

severe due to the inflation of the background thermosphere. Consequently, the resulting escape probability for the clear case reaches ~0.1 at about 174 km, whereas about 190 km in the dusty case. The escape probability for the clear case in the regional dust storm is also larger than that for the dusty case before it reaches ~0.5, but the difference in the altitudes when the probability becomes ~0.1 is about 5 km, implying a milder thermalization of hot O when the regional dust storm occurs.

The altitude of a rapid increase in probabilities from ~0.1 to 0.5 occurs near the region where the collision frequency between hot O and the background thermospheric species becomes small. If a hot O atom maintains its energy higher than the escape energy in this region, the hot O atom is highly likely to escape to space. As shown in Figure 8b, the production rate of escaping hot O peaks at an altitude where the escape probability becomes ~0.1 for each case. Therefore, the probability of escape of hot O from Mars is mainly controlled by an altitude region in the upper atmosphere where the probability become near or larger than ~0.1. This region can be approximately what is traditionally known as a transition region from the collision-dominated to collisionless regime. In our every simulation, we sample the collision frequency, which is the total number of collisions between a hot O atom and the background thermospheric species (*i.e.*, O and CO_2) per second. Figure 8c shows the altitude profiles of sampled collision frequencies for the cases considered. According to our escape probability calculation (Figure 8a), above an altitude of ~170 km, the collisions with ambient thermospheric constituents start having efficient impacts on the escaping population. In the global storm scenarios, the collision frequency in the

dusty case is larger by a factor of about ~1.7 (~2.2 near the subsolar point; not shown in Figure 8c) than that in the clear case. In the regional dust storm, the difference between the dusty and clear cases is not noticeable.

5. Conclusion

In this study, we investigated the dust storm effects on the formation of the hot O corona and escape process of hot O at Mars. The dust storms we considered in this study are the global dust storm, which occurred in 1971-1972, and regional dust storm, which occurred in 2017. We described the dust storm effects by coupling our AMPS model with the MF-MHD model in one-way. We assumed the effects on the thermosphere is the primary response to the increase in dust in the lower atmosphere of Mars. The input ionosphere to the AMPS model was pre-simulated by the MF-MHD for the dusty and clear atmospheric condition cases for the global and regional storm scenarios, respectively. The sub-coupling-step in our model integration framework was conducted to include the hot O corona simulated by the AMPS model in the computation by the MF-MHD model.

The estimated global photochemical escape rates of hot O for the global dust storm scenario are 2.8×10^{25} s^{-1} and 3.9×10^{25} s^{-1} for the dusty and clear atmospheric condition cases, respectively. For the regional dust storm scenario, the escape rates are 2.1×10^{25} s^{-1} and 2.2×10^{25} s^{-1} for the dusty and clear atmospheric condition cases, respectively. Our integrated model framework predicts that the photochemical escape is decreased by ~28 % when the global dust

storm occurs, whereas this suppression is minimal when the storm is regional. The ionospheres during the dusty cases are shifted upward in altitude, resulting in higher production of hot O at all altitude above the ionospheric peak altitude than that in the clear cases. However, our simulations show that thermalization of hot O via collisions with the inflated thermosphere is severe enough to suppress the increased population of hot O. This decrease is small in the regional dust storm scenario as the inflations of the thermosphere as well as the ionosphere are not significant, compared to the global dust storm scenario. If there is a global dust storm during which MAVEN is able to detect the O 130.4-nm emission, we expect to observe ~28 % decrease in the O 130.4-nm brightness as exospheric O is optically thin (*i.e.,* emission brightness is linearly correlated with the magnitude of the density). Interestingly, when the Martian thermosphere is heated by the enhanced solar EUV radiation at the early epoch, we also find the photochemical loss of hot O decreased due to the enhanced collisions between hot O and the thermospheric background gas [*Dong et al.,* 2018]

We also conducted an academic exercise with the newly calculated O-CO_2 collision cross section to examine the impacts of inelastic scattering between hot O and thermal CO_2. When inelastic scattering was ignored, which was an artificial test case, the thermalization of hot O for the dusty cases does not occur efficiently for both storm scenarios, resulting in higher escape rates than those for the clear atmospheric condition cases. This exercise demonstrated that both elastic and inelastic scattering between hot O and thermal CO_2 need to be treated appropriately to obtain meaningful estimations for the hot O corona and photochemical escape rate.

The main controlling factors of the changes in escape rate of hot O are production rate of hot O (*i.e.*, dissociative recombination rate of O_2^+ with electrons) and collision frequency of hot O with the background thermosphere. The combination of these two factors determines the net global escape rate. Our dust storm simulations demonstrated that the relation between production and collisional frequency of hot O in the transition region from collision-dominated to collisionless regimes is critical to the net escape of hot O. This study examined only the effects of the dust increase in the lower atmosphere of Mars, which is described as the inflation of the thermosphere and ionosphere, on the resulting hot O corona and photochemical escape. Other processes can also affect the photochemical escape processes of hot O and induce similar variability in escape rate and the hot O density. These effects will be investigated in future studies.

http://csem.engin.umich.edu/tools/swmf. The AMPS model results for this study are publicly available at http://dx.doi.org/10.17632/c85kp386fd.1.

References

Bieler, A., Altwegg, K., Balsiger, H., Berthelier, J., Calmonte, U., and Combi, M. et al. (2015). Comparison of 3D kinetic and hydrodynamic models to ROSINA-COPS measurements of the neutral coma of 67P/Churyumov-Gerasimenko. *Astron. Astrophy.,* 583, A7. doi:10.1051/0004-6361/201526178.

Bird, G. (1994). *Molecular Gas Dynamics and the Direct Simulation Monte Carlo Method.* Clarendon Press.

Bockelée-Morvan, D., Debout, V., Erard, S., Leyrat, C., Capaccioni, F., and Filacchione, G. et al. (2015). First observations of H2O and CO2 vapor in comet 67P/Churyumov-Gerasimenko made by VIRTIS onboard Rosetta, *Astron. Astrophy.,* 583, A6. doi:10.1051/0004- 6361/201526303.

Bougher, S. W., J. Murphy, and R. M. Haberle (1997), Dust storm impacts on the Mars upper atmosphere, *Adv. Space Res.*, 19, 8. pp. 1255-1260.

Cantor, B.A., James, P.B., Caplinger, M., Wolff, M.J., 2001. Martian dust storms: 1999 Mars Orbiter Camera observations. *J. Geophys. Res.,* 106, 23653–23687.

Combi, M., Tenishev, V., Rubin, M., Fougere, N., and Gombosi, T. (2012). Narrow dust jets in a diffuse gas coma : A natural product of small active regions on comets. *Astrophys. J.,* 749(1), 29. doi:10.1088/0004-637x/749/1/29.

Cravens, T. E., A. Rahmati, Jane L. Fox, R. Lillis, S. Bougher, J. Luhmann, S. Sakai, J. Deighan, Yuni Lee, M. Combi, and B. Jakosky (2017), Hot oxygen escape from Mars: Simple

scaling with solar EUV irradiance, *J. Geophys. Res.*, 122, 1102, doi:10.1002/2016JA023461.

de Lara-Castells, M. P., M. I. Hernández, G. Delgado-Barrio, P. Villarreal, and M. López-Puertas (2006). Vibrational quenching of $CO_2(010)$ by collisions with $O(^3P)$ at thermal energies: a quantum-mechanical study, *J. Chem. Phys.* 124, doi:10.1063/1.2189860.

Dong, C. F., S. W. Bougher, Y. J. Ma, G. Toth, Y. Lee, A. F. Nagy et al. (2015), Solar wind interaction with the Martian upper atmosphere: Crustal field orientation, solar cycle and seasonal variations, *J. Geophys. Res. Space Physics*, 120, 7857--7872, doi:10.1002/2015JA020990.

Dong, C. F., S. W. Bougher, Y. J. Ma, Y. Lee, G. Toth, A. F. Nagy et al. (2018), Solar wind interaction with the Martian upper atmosphere: Roles of the cold thermosphere and hot oxygen corona, *J. Geophys. Res. Space Physics*, 123, 6639-6654, doi:10.1029/2018ja025543.

Dong, C. F., S. W. Bougher, Y.J. Ma, G. Toth, A.F. Nagy, and D. Najib (2014), Solar wind interaction with Mars upper atmosphere: Results from the one-way coupling between the multi-fluid MHD model and the M-TGCM model, *Geophys. Res. Lett.*, 41, 2708-2715, doi:10.1002/2014GL059515.

C. F. Dong, Y. Lee, Y. J. Ma, M. Lingam, S. W. Bougher, J. G. Luhmann et al. (2018), Modeling Martian Atmospheric Losses over Time: Implications for Exoplanetary Climate Evolution and Habitability, *Astrophys. J. Letters*, 859, L14.

Fang, X., et al. (2019), Mars Dust Storm Effects in the Ionosphere and Magnetosphere and Implications for Atmospheric Carbon Loss, *J. Geophys. Res. Space Phys*. 2019JA026838.

Fang, X., S. W. Bougher, R. E. Johnson, J. G. Luhmann, Y. Ma, Y. -C. Wang, and M. W. Liemohn (2013), The importance of pickup oxygen ion precipitation to the Mars upper atmosphere under extreme solar wind conditions, *Geophys. Res. Lett.,* 40, 1922–1927, doi:10.1002/grl.50415.

Fougere, N., Altwegg, K., Berthelier, J., Bieler, A., Bockelée-Morvan, D., & Calmonte, U. et al. (2016a). Three-dimensional direct simulation Monte-Carlo modeling of the coma of comet 67P/Churyumov-Gerasimenko observed by the VIRTIS and ROSINA instruments on board Rosetta. *Astron. Astrophys.,* 588, A134. doi:10.1051/0004-6361/201527889.

Fougere, N., Altwegg, K., Berthelier, J., Bieler, A., Bockelée-Morvan, D., and Calmonte, U. et al. (2016b). Direct Simulation Monte Carlo modelling of the major species in the coma of comet 67P/Churyumov-Gerasimenko. *Mon. Not. Roy. Astr. Soc.,* 462(Suppl 1), S156-S169. doi:10.1093/mnras/stw2388.

Fougere, N., Combi, M., Tenishev, V., Rubin, M., Bonev, B., and Mumma, M. (2012). Understanding measured water rotational temperatures and column densities in the very innermost coma of Comet 73P/Schwassmann-Wachmann 3 B. *Icarus,* 221(1), 174-185. doi:10.1016/j.icarus.2012.07.019.

Fox, J. L., and A. B. Hać (2009), Photochemical escape of oxygen from Mars: A comparison of the exobase approximation to a Monte Carlo method, *Icarus*, 204, 527-544, doi:10.1016/j.icarus.2009.07.005.

Fox, J. L., and A. B. Hać (2014), The escape of O from Mars: Sensitivity to the elastic cross sections, *Icarus,* 228, 375-385, doi:10.1016/j.icarus.2013.10.014.

G.A. Briggs, W.A. Baum, and J. Barnes (1797), Viking Orbiter imaging observations of dust in the Martian atmosphere, *J. Geophys. Res.,* 84 (1979), pp. 2795-2820.

Gacesa, M., N. Lewkow, V. Kharchenko (2017), Non-thermal production and escape of OH from the upper atmosphere of Mars, *Icarus*, 284, 90-96.

Gacesa, M., R. J. Lillis, and K. J. Zahnle (2019a), $O(^3P)+CO_2$ scattering cross sections at superthermal collision energies for planetary aeronomy, arXiv:1906.11368.

Gacesa, M., R. J. Lillis, and K. J. Zahnle (2019b), $O(^3P)+CO_2$ scattering cross sections at superthermal collision energies for planetary aeronomy: Raw data pre-release (Version v0.9-beta) [Data set]. Zenodo. http://doi.org/10.5281/zenodo.3256699

Gröller, H., H. Lichtenegger, H. Lammer, and V. I. Shematovich (2014), Hot oxygen and carbon escape from the Martian atmosphere, *Planet. Space Sci.,* 98, 93–105, doi:10.1016/j.pss.2014.01.007.

Hutson, J. M., and S. Green (1994). MOLSCAT Version 14, Collaborative Computational Project 6 (distributed by Collaborative Computational Project No. 6 of The Engineering and Physica Sciences Research Council (UK)).

Jakosky, B., et al. (2015), The 2013 Mars Atmosphere and Volatile EvolutioN (MAVEN) mission to Mars, *Space Sci. Rev.*, doi:10.1007/s11214-015-0139-x.

Kharchenko, V., A. Dalgarno, B. Zygelman, and J. –H. Yee (2000), Energy transfer in collisions of oxygen atoms in the terrestrial atmosphere, *J. Geophys. Res.,* 105, A11, 24,899-24,906.

Lee et al. (2018b), Updated Estimations of Distribution and Photochemical Escape Rate of O, *MAVEN Project Science Group meeting*.

Lee, Y., C. Dong, D. Pawlowski, E. Thiemann, V. Tenishev, P. Mahaffy et al. (2018). Effects of a solar flare on the Martian hot O corona and photochemical escape. *Geophys. Res. Lett.*, 45, 6814–6822, doi:10.1029/2018GL077732.

Lee, Y., et al. (2015a), A comparison of 3-D model predictions of Mars' oxygen corona with early MAVEN IUVS observations, *Geophys. Res. Lett.*, 42, doi:10.1002/2015GL065291.

Lee, Y., M. R. Combi, V. Tenishev, and S. W. Bougher (2014a), Hot carbon corona in Mars' upper thermosphere and exosphere: 1. Mechanisms and structure of the hot corona for low solar activity at equinox, *J. Geophys. Res. Planets*, 119, 905–924, doi:10.1002/2013JE004552.

Lee, Y., M. R. Combi, V. Tenishev, and S. W. Bougher (2014b), Hot carbon corona in Mars' upper thermosphere and exosphere: 2. Solar cycle and seasonal variability, *J. Geophys. Res. Planets*, 119, 2487–2509, doi:10.1002/2014JE004669.

Lee, Y., M. R. Combi, V. Tenishev, S. W. Bougher, and R. J. Lillis (2015b), Hot oxygen corona at Mars and the photochemical escape of oxygen: Improved description of the thermosphere, ionosphere, and exosphere, *J. Geophys. Res. Planets*, 120, 1880–1892, doi:10.1002/2015JE004890.

Lillis, R. J., et al. (2017), Photochemical escape of oxygen from Mars: First results from MAVEN in situ data, *J. Geophys. Res. Space Physics*, 122, 3815–3836, doi:10.1002/2016JA023525.

Mahaffy, P. R., et al. (2014), The neutral gas and ion mass spectrometer on the Mars atmosphere and volatile evolution mission, *Space Sci. Rev.*, 195(1), 49–73, doi:10.1007/s11214-014-0091-1.

McClintock, W. E., N. M. Schneider, G. M. Holsclaw, A. C. Hoskins, I. Stewart, J. Deighan, J. T. Clarke, F. Montmessin, and R. V. Yelle (2014), The Imaging Ultraviolet Spectrograph (IUVS) for the MAVEN mission, *Space Sci. Rev.*, doi:10.1007/s11214-014-0098-7.

Morschhauser, A., V. Lesur, and M. Grott (2014), A spherical harmonic model of the lithospheric magnetic field of Mars, *J. Geophys. Res. Planets*, 119, 1162–1188, doi:10.1002/2013JE004555.

Nagy, A. F., M. W. Liemohn, J. L. Fox, and J. Kim (2001), Hot carbon densities in the exosphere of Mars, *J. Geophys. Res.,* 106, 21,565-21,568.

Najib, D., A. F. Nagy, G. Toth, Y.J. Ma (2011), Three-dimensional, multifluid, high spatial resolution MHD model studies of the solar wind interaction with Mars, *J. Geophys. Res. Space Physics*, 116, A05204, doi:10.1029/2010JA016272.

Pabari, J. P., and P. J. Bhalodi (2017) Estimation of micrometeorites and satellite dust flux surrounding Mars in the light of MAVEN results, *Icarus,* 288, 1-9, doi:10.1016/j.icarus.2017.01.023.

Rafkin, S. C. R. (2009), A positive radiative-dynamic feedback mechanism for the maintenance and growth of Martian dust storms, *J. Geophys. Res.*, 114, E01009, doi:10.1029/2008JE003217.

Rahmati, A., D. E. Larson, T. E. Cravens, R. J. Lillis, J. S. Halekas, J. P. McFadden, P. A. Dunn, D. L. Mitchell, E. M. B. Thiemann, F. G. Eparvier, G. A. DiBraccio, J. R. Espley, C. Mazelle, and B. M. Jakosky (2017), MAVEN measured oxygen and hydrogen pickup ions: Probing the Martian exosphere and neutral escape, *J. Geophys. Res.*, 122, 3689, doi:10.1002/2016JA023371.

Rubin, M., Tenishev, V., Combi, M., Hansen, K., Gombosi, T., Altwegg, K., and Balsiger, H. (2011). Monte Carlo modeling of neutral gas and dust in the coma of Comet 1P/Halley. *Icarus,* 213(2), 655-677, doi:10.1016/j.icarus.2011.04.006.

Tenishev, V., Combi, M., Teolis, B., and Waite, J. (2010). An approach to numerical simulation of the gas distribution in the atmosphere of Enceladus. *J. Geophys. Res.,* 115, A09302. doi:10.1029/2009ja015223.

Tenishev, V., M. R. Combi, and B. Davidsson (2008), A Global kinetic model for cometary comae. The evolution of the coma of the Rosetta target comet Churyumov–Gerasimenko throughout the mission, *Astrophys. J.*, 685, 659–677.

Tenishev, V., M. R. Combi, and M. Rubin (2011), Numerical simulation of dust in a cometary coma: Application to comet 67P/Churyumov-Gerasimenko, *Astrophys. J.*, 732, 104, doi:10.1088/0004-637X/732/2/104.

Tenishev, V., M. Rubin, O. J. Tucker, M. R. Combi, and M. Sarantos (2013), Kinetic modeling of sodium in the lunar exosphere, Icarus, 226, 1538–1549, doi:10.1016/j.icarus.2013.08.021.

Tenishev, V., Öztürk, D., Combi, M., Rubin, M., Waite, J., and Perry, M. (2014). Effect of the Tiger Stripes on the water vapor distribution in Enceladus' exosphere. *J. Geophys. Res.,* 119(12), 2658-2667. doi:10.1002/2014je004700.

Thorpe, T. E. (1979). A history of Mars atmospheric opacity in the southern hemisphere during the Viking extended mission, *J. Geophys. Res.*, 84, 6663 – 6683 (1979).

Valeille, A., M. R. Combi, S. W. Bougher, V. Tenishev, and A. F. Nagy (2009b), Three-dimensional study of Mars upper thermosphere/ionosphere and hot oxygen corona: 2. Solar cycle, seasonal variations, and evolution over history, *J. Geophys. Res.,* 114, E11006, doi:10.1029/2009JE003389.

Valeille, A., V. Tenishev, S. W. Bougher, M. R. Combi, and A. F. Nagy (2009a), Three-dimensional study of Mars upper thermosphere/ionosphere and hot oxygen corona: 1.

General description and results at equinox for solar low conditions, *J. Geophys. Res.*, 114, E11005, doi:10.1029/2009JE003388.

Vandaele, A. C., et al. (2019), Martian dust storm impact on atmospheric H_2O and D/H observed by ExoMars Trace Gas Orbiter, *Nature Letter*, 568, pp. 521-525.

Waite, Jr. et al. (2006). Cassini Ion and Neutral Mass Spectrometer: Enceladus Plume Composition and Structure. *Science,* 311(5766), 1419-1422. doi:10.1126/science.1121290.

Wang, J. S., and E. Nielsen (2003), Behavior of the Martian dayside electron density peak during global dust storms. *Planetary and Space Science*, 51(4–5), 329-338. https://doi.org/10.1016/S0032-0633(03)00015-1.

Yagi, M., F. Leblanc, J. Y. Chaufray, F. Gonzalez-Galindo, S. Hess, and R. Modolo (2012), Mars exospheric thermal and non-thermal components: Seasonal and local variations, *Icarus*, 221, 682-693.
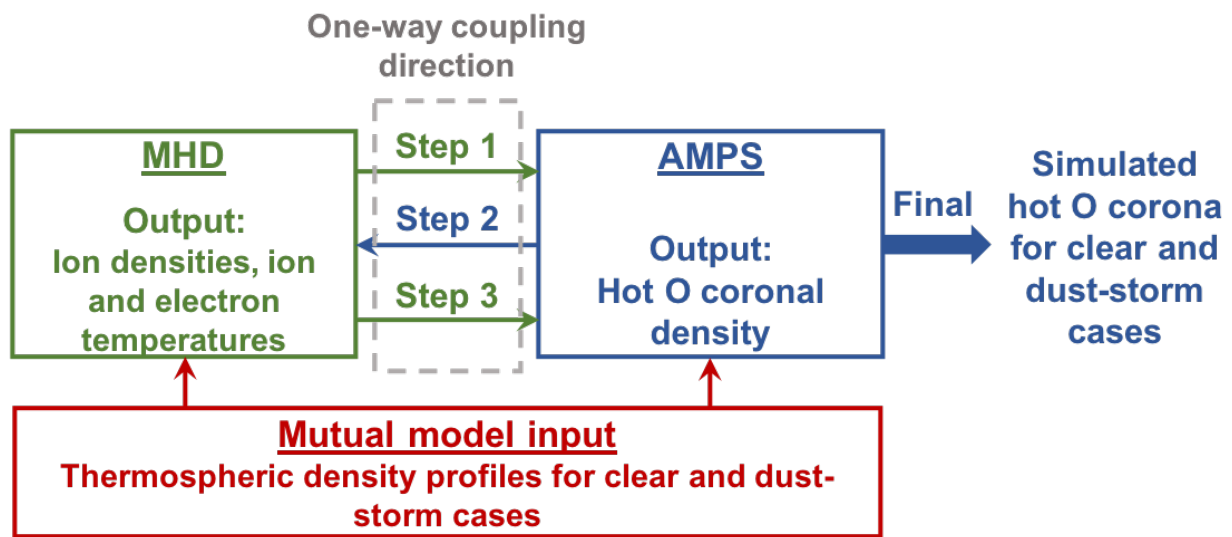
Figure 1. A diagram illustrating our one-way coupling procedure. The arrows indicate the steps of our model integration process as well as direction of the one-way coupling.
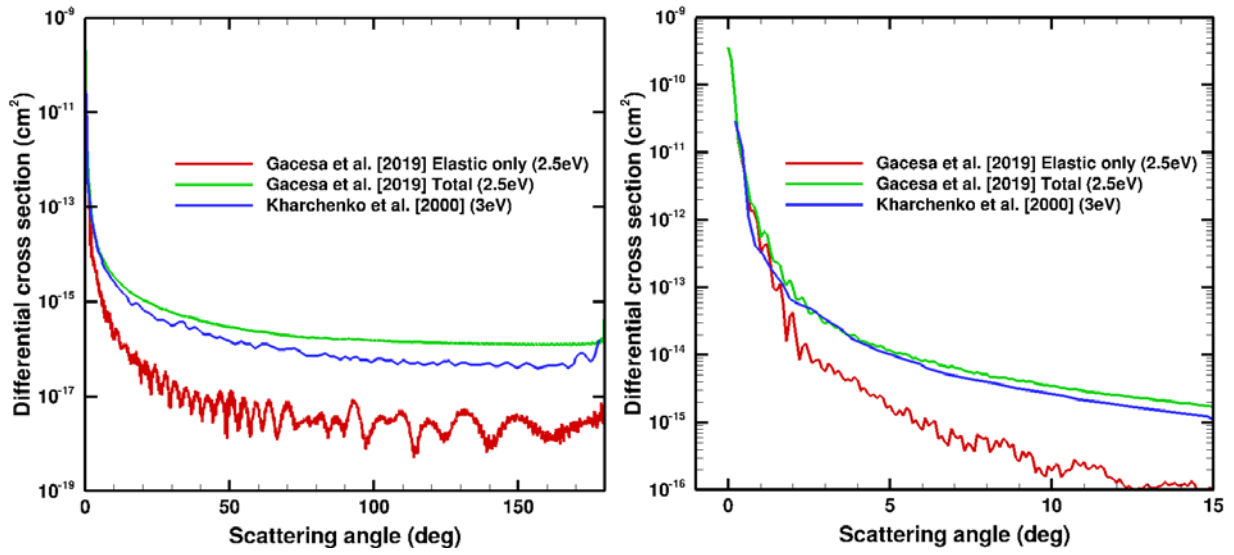
Figure 2. Angular differential cross sections considered for this study for (Left) the entire range

of the scattering angle and (Right) small angles to highlight the forward scattering peaks.
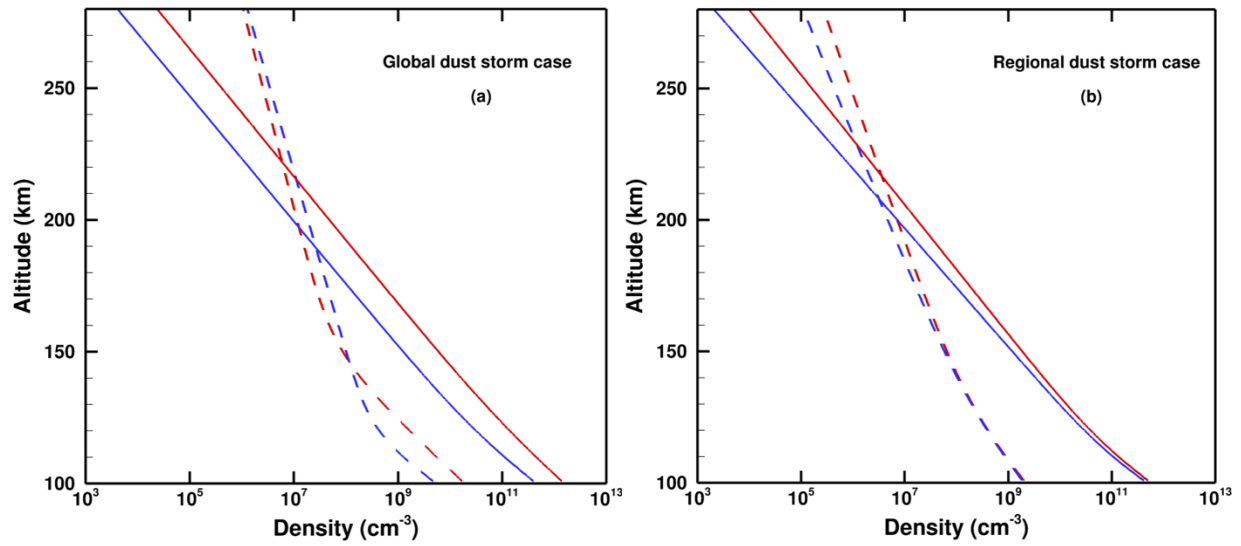
Figure 3. Altitude profiles of the thermospheric densities adopted by the MF-MHD and AMPS models. The O (dashed) and CO2 (solid) for the dusty (red) and clear (blue) cases are shown for the (a) global and (b) regional dust storm scenarios.
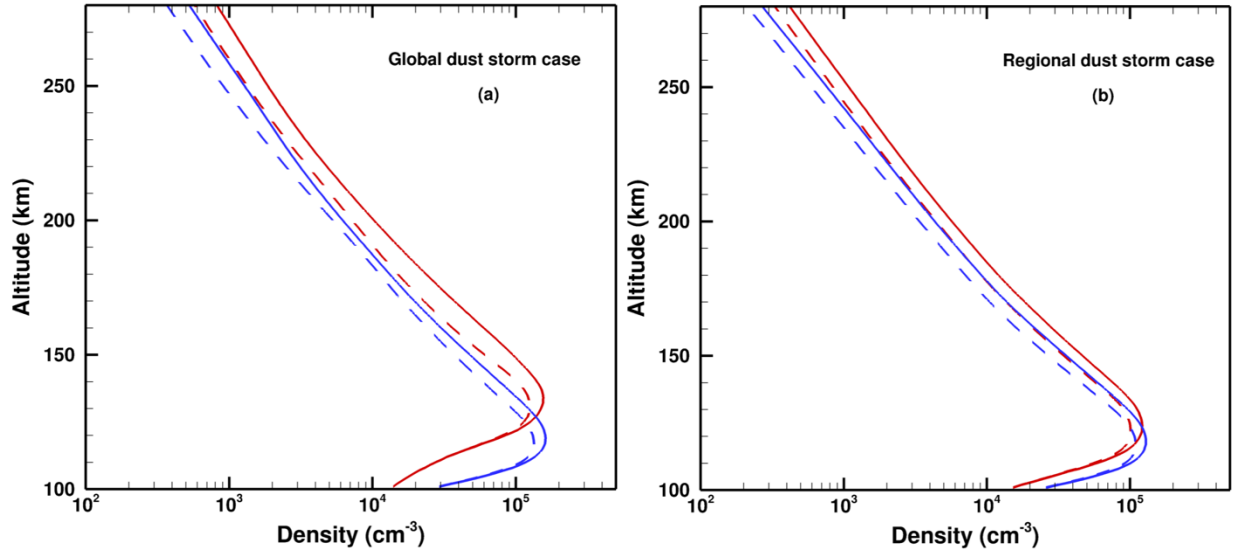
Figure 4. Altitude profiles of the electron and O_2^+ densities computed by the MF-MHD model for the (a) global dust storm and (b) regional dust storm scenarios. Solid lines indicate the electron density, where dash lines are the O_2^+ density. The dusty and clear cases are shown as red and blue, respectively.
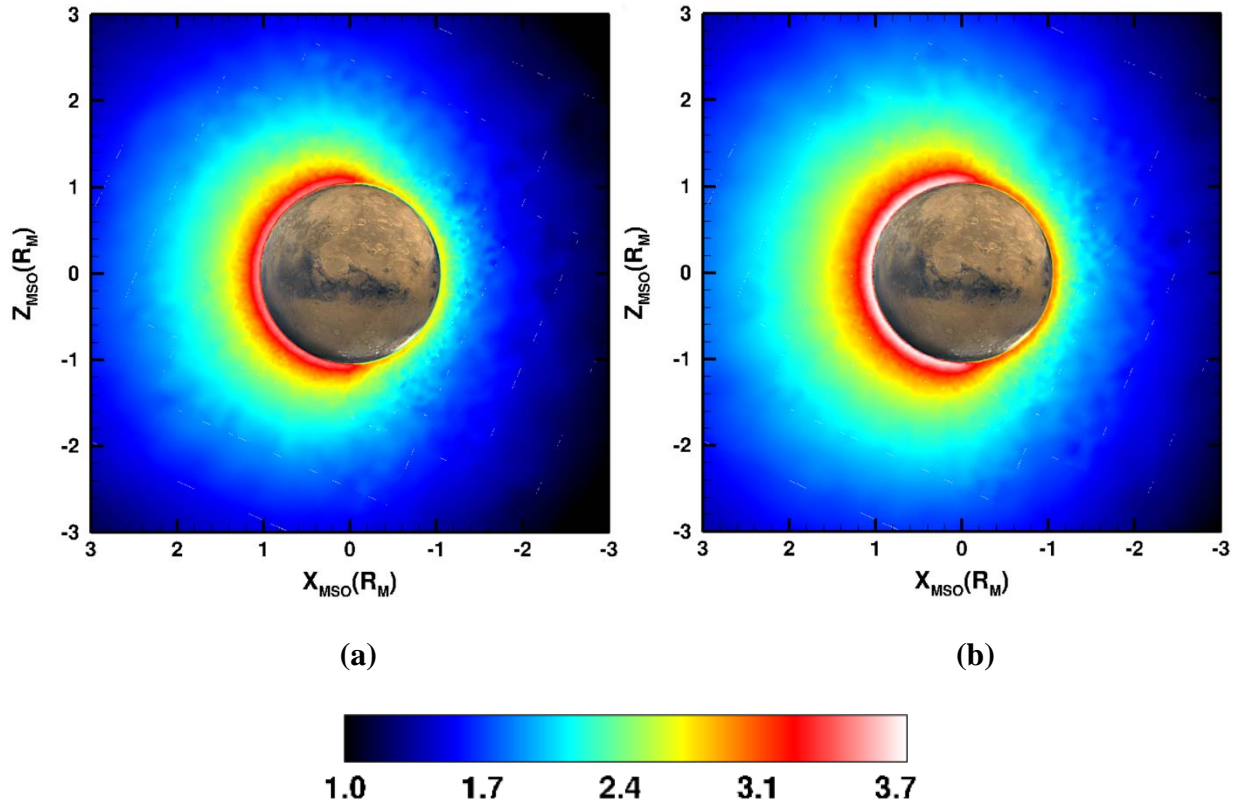
Figure 5. Noon-midnight meridional plane views of the simulated hot O corona for (a) the dusty and (b) clear atmospheric condition cases in the global dust storm scenario. The color contour indicates the log of the hot O density (cm^{-3}). The sun is located where the positive X-axis points.
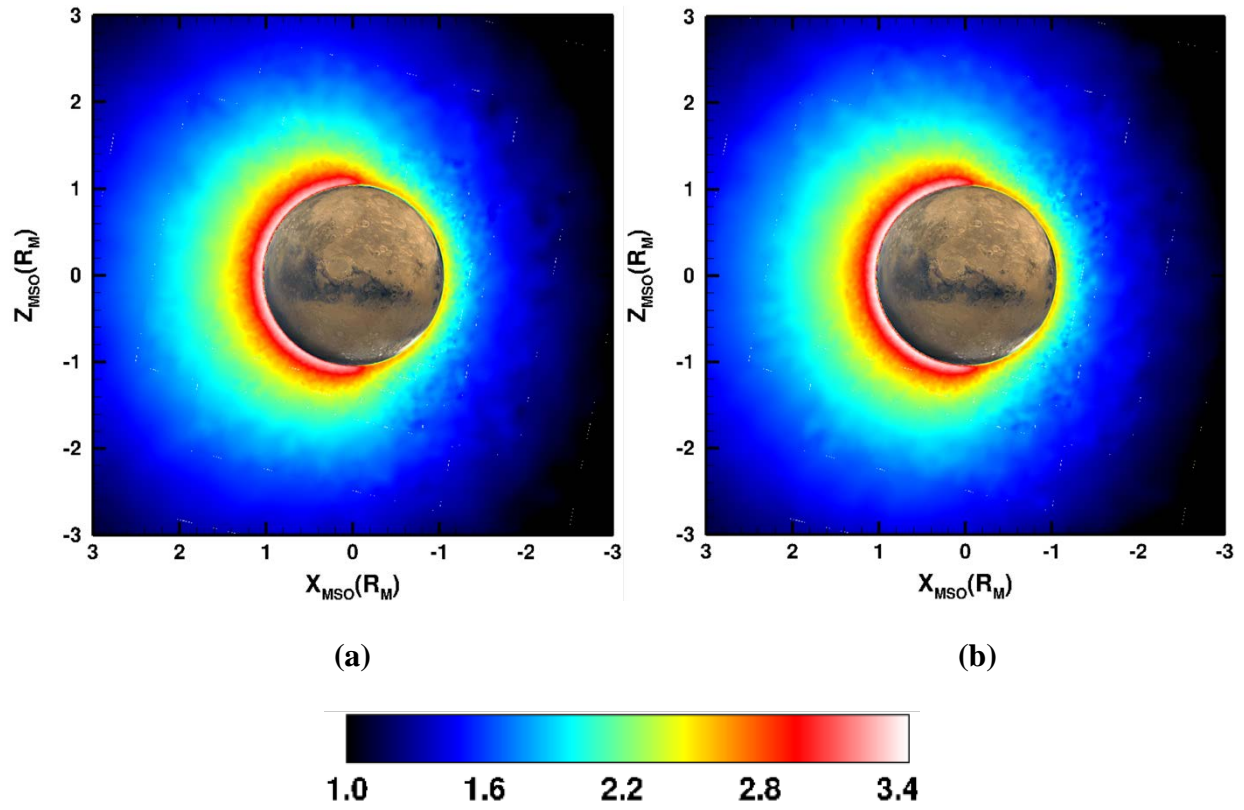
Figure 6. Same as Figure 5 for the regional dust storm scenario.
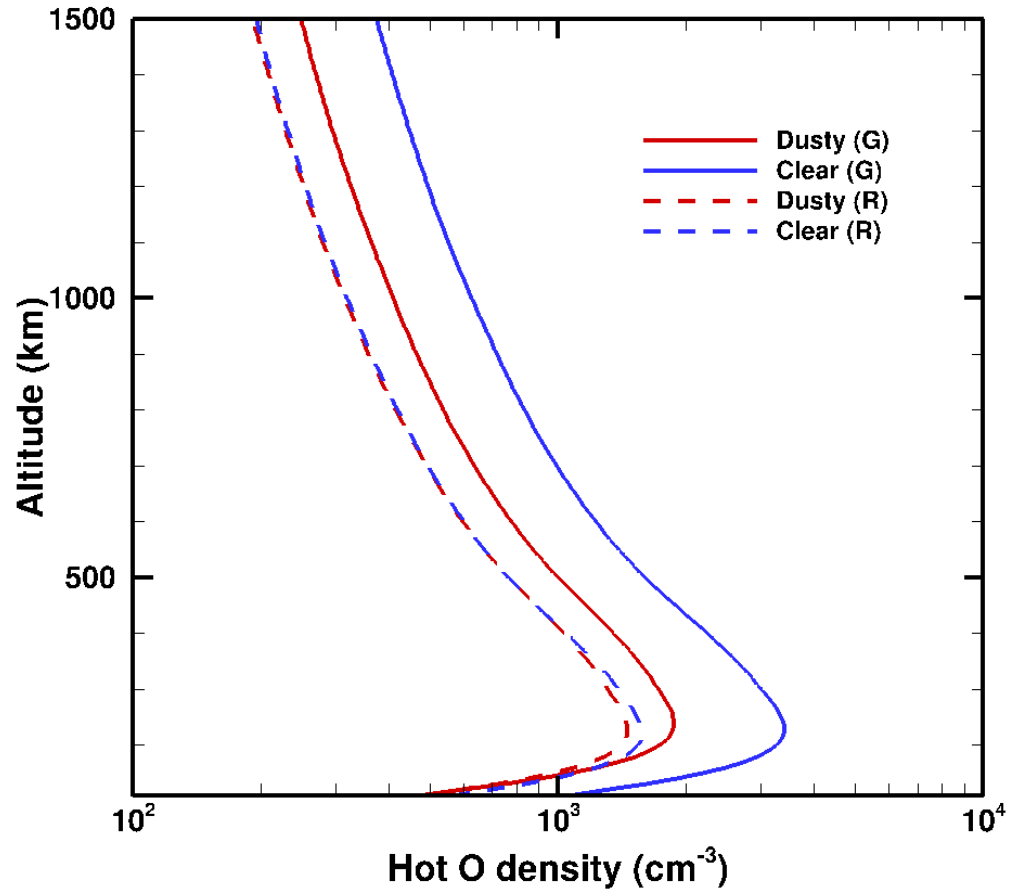
Figure 7. Altitude profiles of the hot O densities for the cases considered. The 3D hot O corona from our AMPS simulations are averaged globally. The solid and dashed lines indicate the global and region dust storm scenarios, respectively. Red and blue represent the dusty and clear cases, respectively.
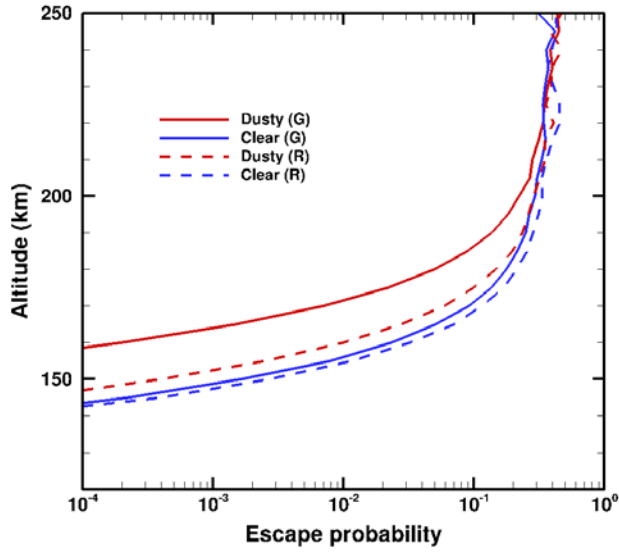
(a)
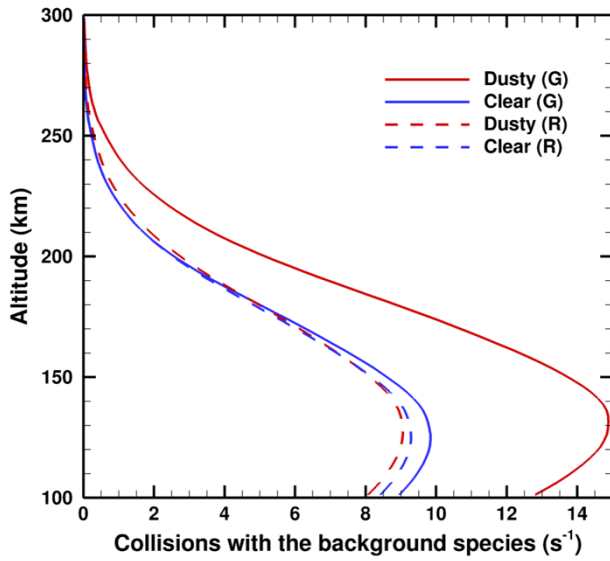
(b)
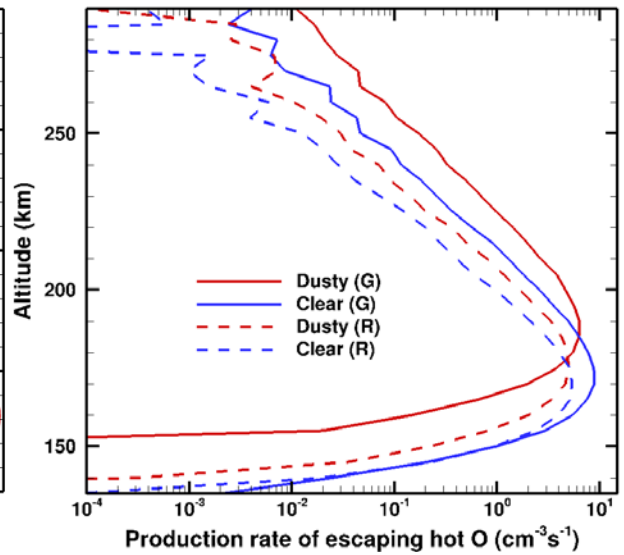
(c)

Figure 8. (a) Escape probabilities computed at a solar zenith angle of 10°, **(b)** number of collisions per hot O atom with the background thermospheric species (*i.e.*, cold O and CO_2), and

(c) production rate of escaping hot O for the cases considered in this study. The line styles and colors indicate the same cases described in Figure 7.
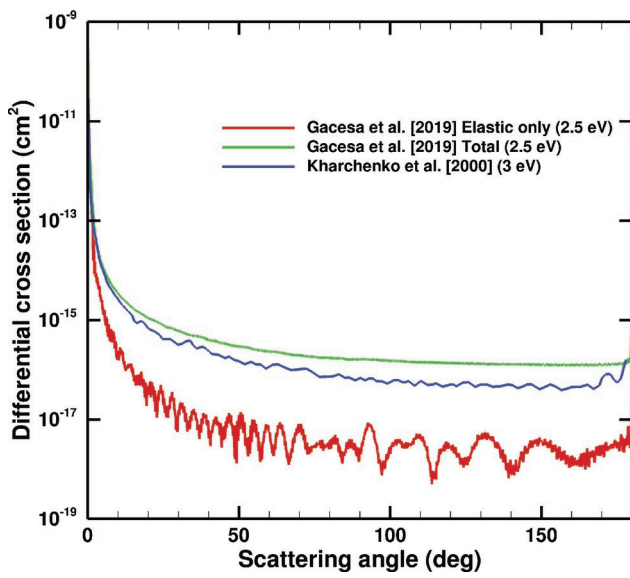
Table 1. Computed escape rate for the cases considered.

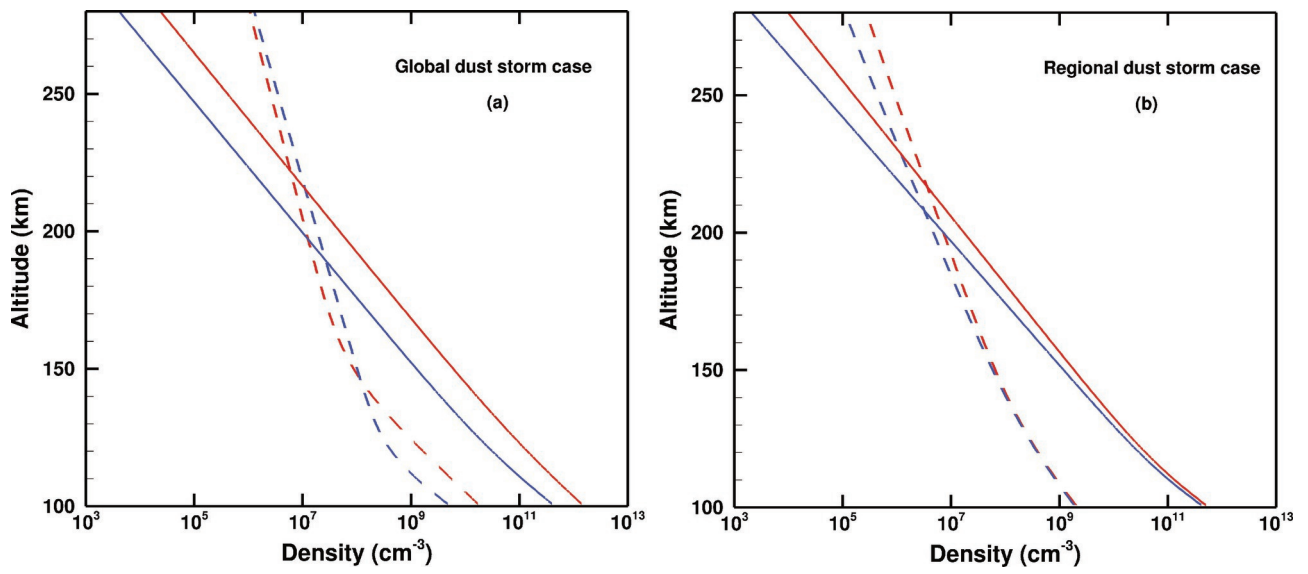| Escape rate (s^{-1})	Global Dusty	Global Clear	Regional Dusty	Regional Clear
Kharchenko et al. [2000]	2.0×10^{25}	2.8×10^{25}	1.4×10^{25}	1.5×10^{25}
Gacesa et al. [2019a] Elastic only*	5.3×10^{26}	4.9×10^{26}	3.9×10^{26}	3.8×10^{26}
Gacesa et al. [2019a] Elastic + Inelastic	2.8×10^{25}	3.9×10^{25}	2.1×10^{25}	2.2×10^{25}

* This cross section, which considers only elastic scattering, is not a realistic estimation. This cross section is used only for this academic exercise to show the impacts of ignoring inelastic scattering between hot O and CO_2.

One-way coupling direction

MHD

Output:
Ion densities, ion and electron temperatures

Step 1

Step 2

Step 3

AMPS

Output:
Hot O coronal density

Final

Simulated hot O corona for clear and dust-storm cases

Mutual model input
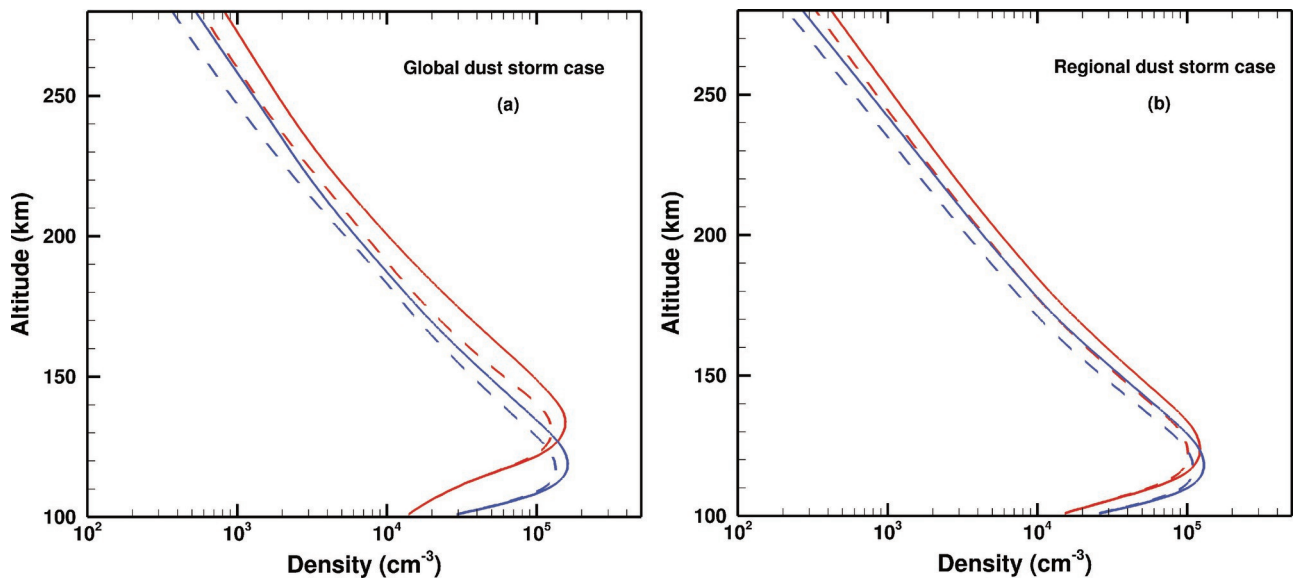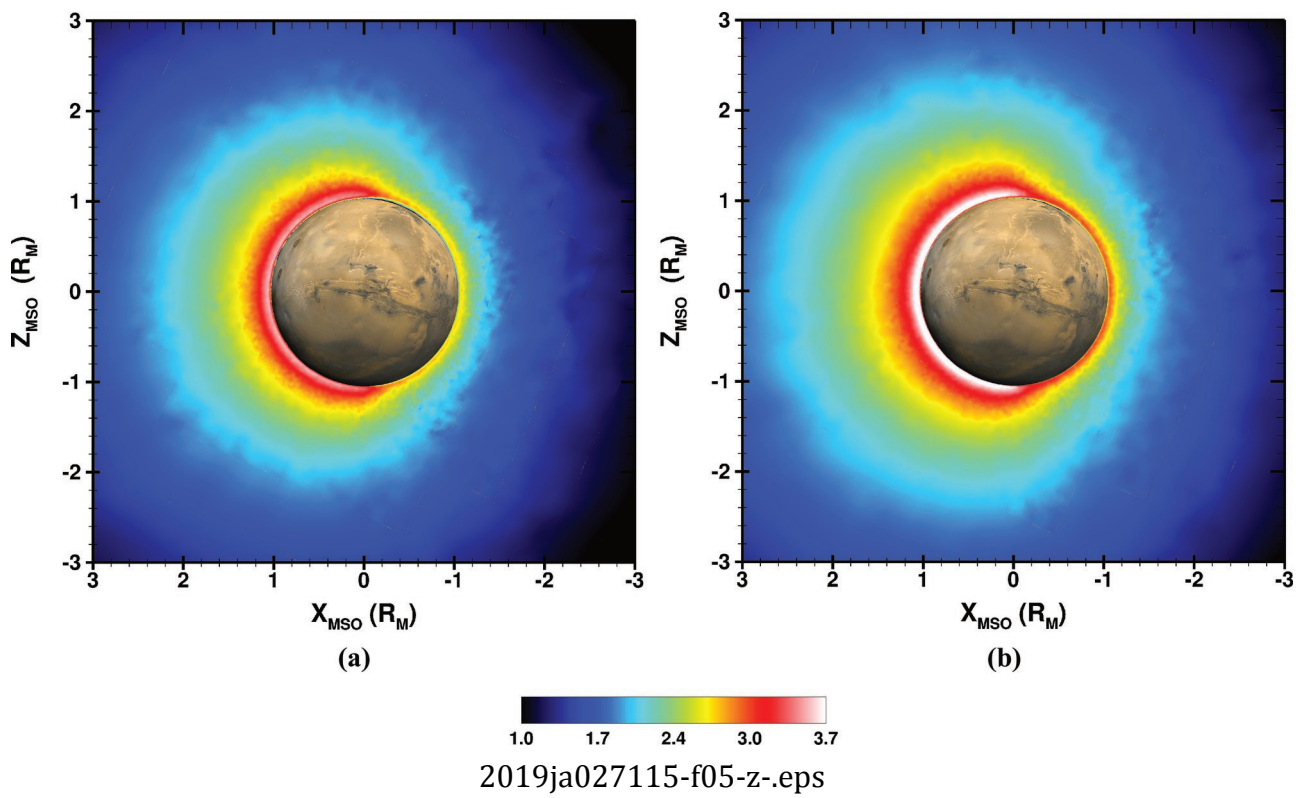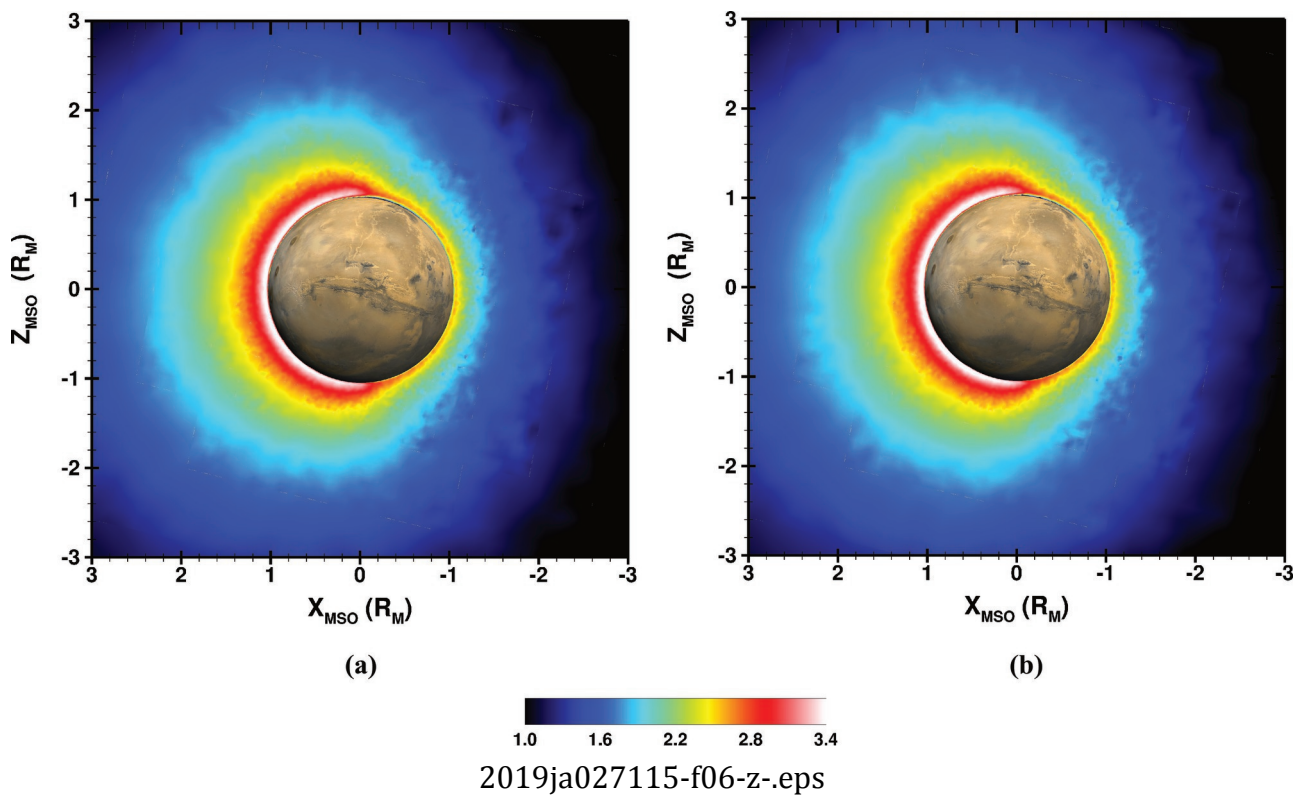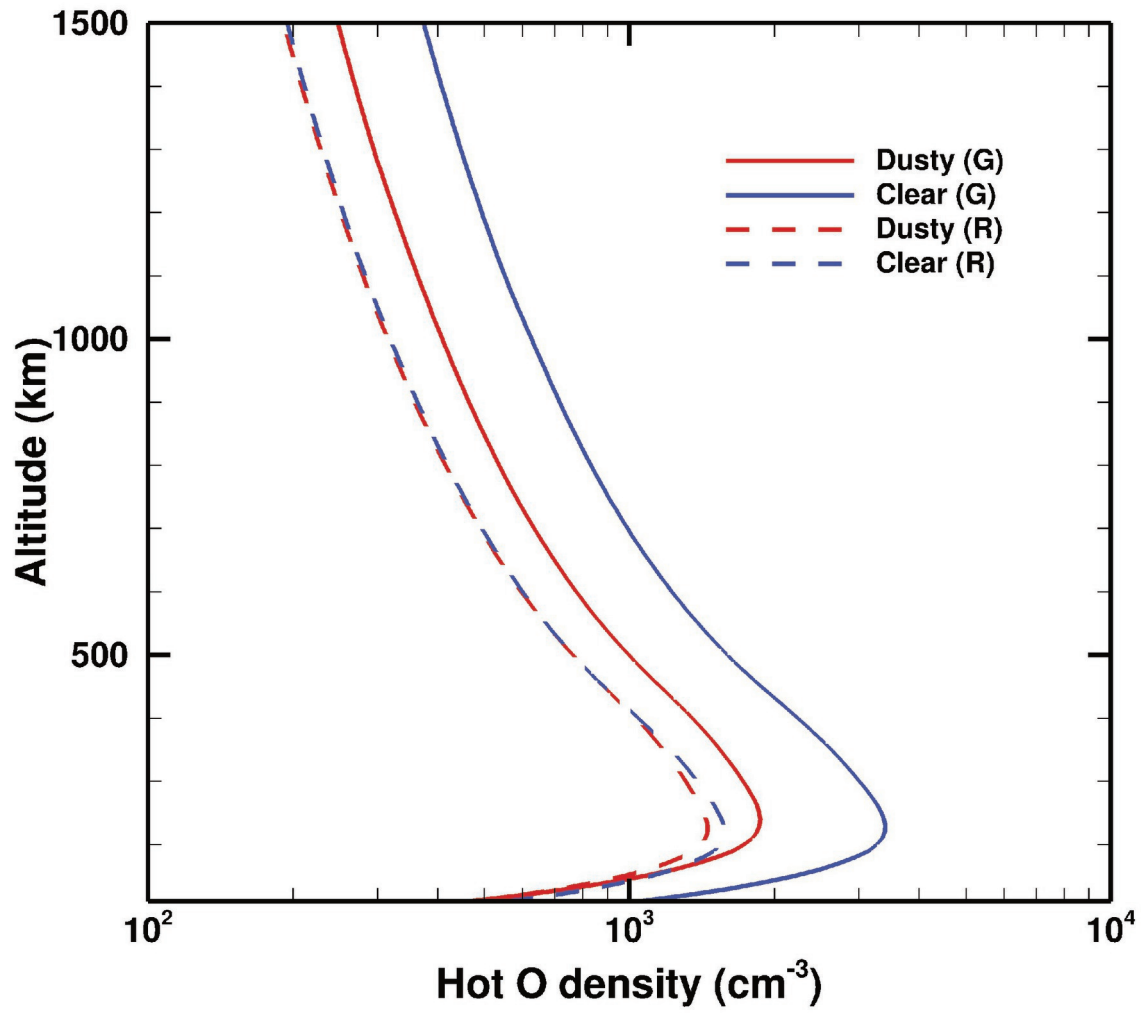Thermospheric density profiles for clear and dust-storm cases
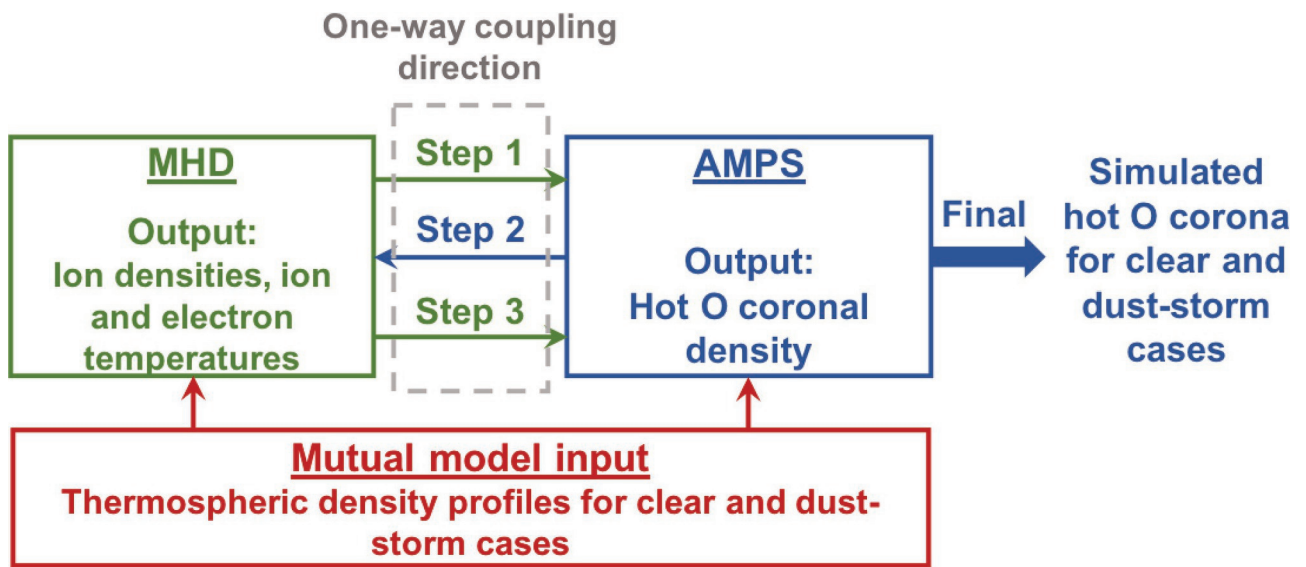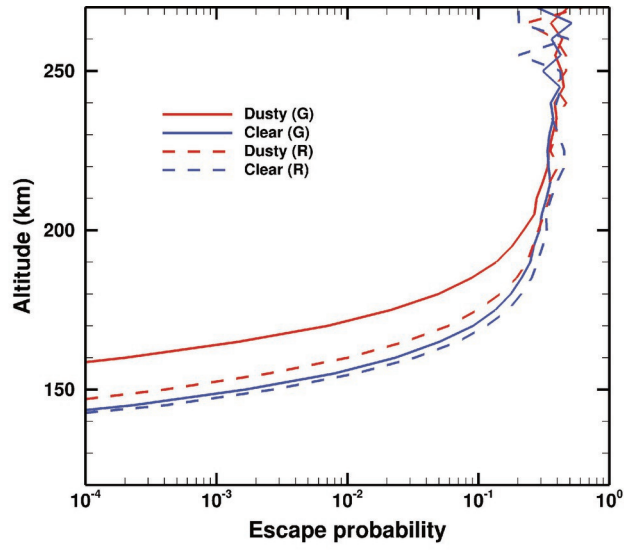
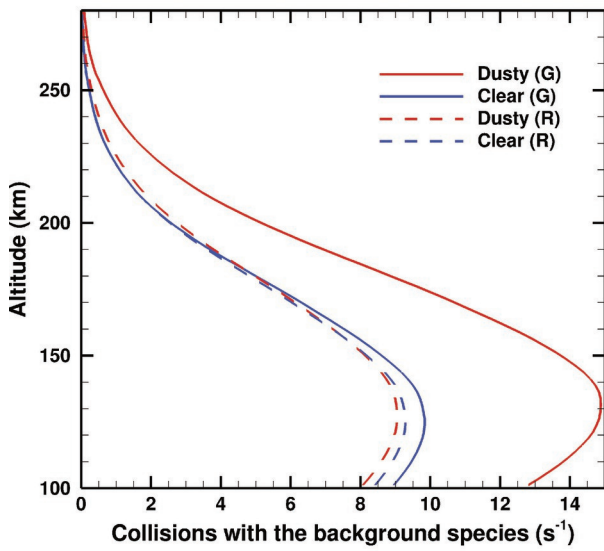2019ja027115-f01-z-.eps
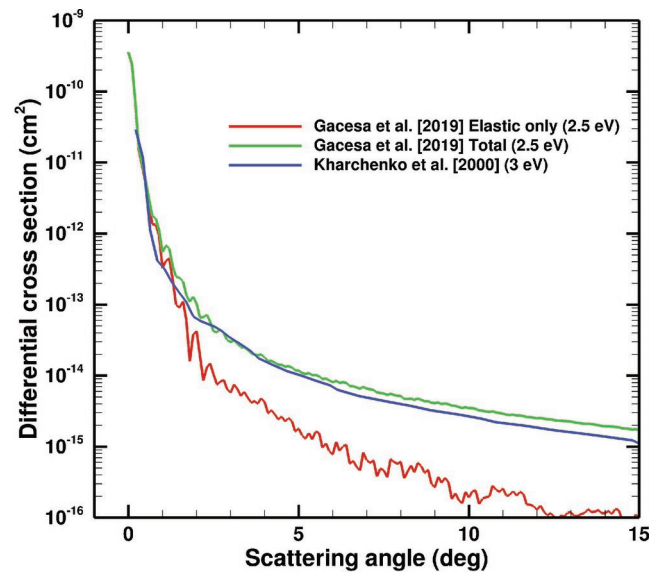
2019ja027115-f02-z-.eps

2019ja027115-f03-z-.eps

Global dust storm case
(a)

Regional dust storm case
(b)

2019ja027115-f04-z-.eps

(a)

(b)

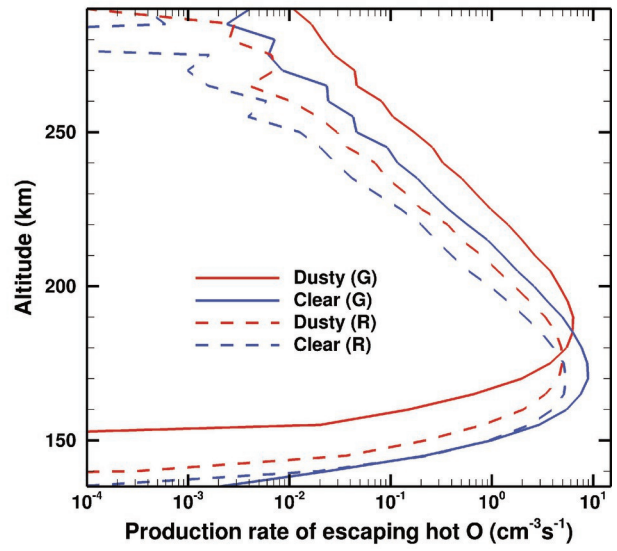1.0   1.7   2.4   3.0   3.7

2019ja027115-f05-z-.eps

(a)   (b)

2019ja027115-f06-z-.eps

Figure: Hot O density (cm^{-3}) versus Altitude (km) showing Dusty (G), Clear (G), Dusty (R), and Clear (R).

2019ja027115-f07-z-.eps

(a)

(b)

(c)

2019ja027115-f08-z-.eps